

NormalView: sensor-agnostic tree species classification from backpack and aerial lidar data using geometric projections

Preprint – December 8, 2025

Juho Korkeala^{1,*}, Jesse Muhojoki¹, Josef Taher¹, Klaara Salolahti¹, Matti Hyyppä¹, Antero Kukko^{1,2}, Juha Hyyppä^{1,2}

¹*Department of Remote Sensing and Photogrammetry, Finnish Geospatial Research Institute FGI, The National Land Survey of Finland, Vuorimiehentie 5, FI-02150, Espoo, Finland*

²*Department of Built Environment, School of Engineering, Aalto University, P.O. Box 11000, FI-00076, Espoo, Finland*

Abstract

Laser scanning has proven to be an invaluable tool in assessing the decomposition of forest environments. Mobile laser scanning (MLS) has shown to be highly promising for extremely accurate, tree level inventory. In this study, we present NormalView, a sensor-agnostic projection-based deep learning method for classifying tree species from point cloud data. NormalView embeds local geometric information into two-dimensional projections, in the form of normal vector estimates, and uses the projections as inputs to an image classification network, YOLOv11. In addition, we inspected the effect of multispectral radiometric intensity information on classification performance. We trained and tested our model on high-density MLS data (7 species, ~5000 pts/m²), as well as high-density airborne laser scanning (ALS) data (9 species, >1000 pts/m²). On the MLS data, NormalView achieves an overall accuracy (macro-average accuracy) of 95.5 % (94.8 %), and 91.8 % (79.1 %) on the ALS data. We found that having intensity information from multiple scanners provides benefits in tree species classification, and the best model on the multispectral ALS dataset was a model using intensity information from all three channels of the multispectral ALS. This study demonstrates that projection-based methods, when enhanced with geometric information and coupled with state-of-the-art image classification backbones, can achieve exceptional results. Crucially, these methods are sensor-agnostic, relying only on geometric information. Additionally, we publically release the MLS dataset used in the study.

Keywords Tree species classification, Point cloud, Mobile laser scanning, Backpack laser scanning, Deep learning, YOLO, Multispectral ALS

1 Introduction

Tree species classification is a key tool in understanding forest and urban ecosystems. Understanding the composition of species helps monitor biodiversity, manage forest risks, and to understand the ecological richness of forest environments (Chirici et al., 2012; Gamfeldt et al., 2013; Huuskonen et al., 2021). Accurate species classification also has economical impact (Haara et al., 2019). In boreal forests, it is found that aspen (*Populus tremula*) holds an important role as a keystone species (Kivinen et al., 2020; Kouki et al., 2004), serving as a biodiversity hotspot hosting hundreds of species, including woodpeckers and flying squirrels (Angelstam and Mikusiński, 1994; Tikkanen et al., 2006; Remm et al., 2017). In recent years, automated forest inventory has started to replace more traditional methods in forest inventory. Recently, we have seen deep learning-based methods for semantic segmentation of forests (see e.g. Wielgosz et al. (2024); Henrich et al. (2024); Ruoppa et al. (2025); Xiang et al. (2025)). In combination, these segmentation methods and species classification methods can provide us with forest information almost completely automated.

Mobile laser scanning (MLS) and airborne laser scanning (ALS) have proven to be invaluable tools in forestry. The applications of MLS include estimation of stem curves (Hyyppä et al., 2020), extracting branch information (Winberg et al., 2023), and collecting forest inventories (Liang et al., 2014).

ALS data has been used for individual tree detection and their characteristics' assessment (Hyyppä and Inkinen, 1999), height growth (Hyyppä et al., 2003), change detection (Yu et al., 2004), biomass estimations (Dalponte et al., 2018) and semantic segmentation of forests (Ruoppa et al., 2025). Both data types have been used for the classification of tree species (Puliti et al., 2025b; Taher et al., 2025). MLS data is becoming more available with the development of new data collection methods and has significant potential in high-detail analysis of forests.

To classify trees from point cloud data, various methods have been presented previously. The methods utilising artificial intelligence can be roughly divided into three categories: machine learning based-methods, projection-based deep learning methods, and point-based 3D deep learning methods. Machine learning (ML) methods derive handcrafted features from tree point clouds, such as tree height, crown area, height percentiles and intensity and reflectance statistics. For an extensive review of various features used in tree species classification, see Koenig and Höfle (2016). Common ML classifiers include random forests (Breiman, 2001), support vector machines (Cortes and Vapnik, 1995), and linear discriminant analysis (Izenman, 2013). These algorithms have been successfully applied in several tree species classification studies, for example by Hakula et al. (2023); Dalponte et al. (2012); Ørka et al. (2012); Tockner et al. (2025); Yu et al. (2017) for random forests, by Dalponte et al. (2012); Ørka et al. (2012) for support vector machines, and by Ørka et al. (2012); Hardenbol et al. (2021) for linear discriminant analysis.

*Corresponding author: Juho Korkeala (juho.korkeala@nls.fi)

The recent rapid developments in the field of deep learning (DL) have made DL methods surpass more traditional ML methods, as seen in the benchmarks by Puliti et al. (2025b) and Taher et al. (2025). Projection-based methods operate by creating two-dimensional representations of tree point clouds, for example by taking orthographic projection images from multiple angles and colouring the images black-and-white (B&W) (Marinelli et al., 2022; Seidel et al., 2021; Blackburn et al., 2025; Puliti et al., 2025b; Taher et al., 2025), according to depth (Allen et al., 2022), intensity (Blackburn et al., 2025) or geometric features (Blackburn et al., 2025). The classification task is largely studied in the field of image-based artificial intelligence, and one benefit of the 2D-models is the performance of state-of-the-art image models, such as YOLO (Jocher et al., 2023).

3D-DL models operate directly on the point clouds, taking as input subsampled point coordinates and possible additional attributes, such as intensity and reflectance values. The pioneers of deep learning in the realm of point cloud understanding were PointNet (Qi et al., 2017a) and PointNet++ (Qi et al., 2017b). Several studies have shown their ability to classify tree species (Liu et al., 2022a,b; Sun et al., 2023; Liu et al., 2022c; Taher et al., 2025; Puliti et al., 2025b). Newer 3D-architectures include PointMLP (Ma et al., 2022), 3D-convolution models (Tran et al., 2015), graph-based methods (Wang et al., 2019) and transformer-based architectures (Zhao et al., 2021). All of these architectures have been utilised to classify tree species: Liu et al. (2022c,b) used PointMLP, 3D-convolution-based methods were utilised by Liu et al. (2021, 2022c); Puliti et al. (2025b), graph-based methods by Liu et al. (2022c); Puliti et al. (2025b), and transformer-based architectures were applied in Sun et al. (2023); Taher et al. (2025). These studies show the prominence of 3D methods in tree species classification.

Recently, two benchmark studies on tree species classification have been published, namely one by Puliti et al. (2025b) and another by Taher et al. (2025). The former is carried out on the FOR-species20k¹ public dataset (Puliti et al., 2025a), and the other on the MS-ALS-SPECIES² dataset (Hyypä et al., 2025). The FOR-species20k dataset contains more than 20 000 samples from 33 species, which are gathered by different methods (terrestrial laser scanning, MLS, unmanned ALS). In their study, Puliti et al. (2025b) found that image-based models outperformed certain point-based 3D models. In contrast, Taher et al. (2025) found that point-based 3D models, especially transformer-based architectures, outperform image-based models. Hence, it seems currently unclear whether the best classification performance can be achieved by projection-based methods or 3D-architectures.

Normal vector estimations are regularly used in computer vision and point cloud-based applications, for example in segmentation (Yang and Lee, 1999), shape modelling (Pauly et al., 2003) and point cloud registration (Serafin and Grisetti, 2015). However, in point cloud classification problems, especially in forestry related fields, the use of normal information has not been studied.

To address these gaps, this study investigates the potential of

projection-based deep learning methods for tree species classification from point cloud data. We evaluate the suitability of integrating geometric information into projection images through surface normal vector estimation and assess how effectively geometric cues alone can support species classification compared to radiometry-based approaches. Furthermore, we examine the influence of multispectral intensity information from multiple scanners and test model performance across both mobile and airborne laser scanning datasets.

The original contributions of this study are the following:

- We present NormalView, a sensor-agnostic projection-based deep learning method for classifying tree species from point cloud data. NormalView embeds local geometric information into two-dimensional projections, in the form of normal vector estimates, and uses the projections as inputs to an image classification network.
- We extensively inspect the effect of radiometric information on tree species classification via projection-based methods. We compare images coloured by intensity to projections done without intensity information, as well as examine the effect of multispectral intensity information compared to single channel intensity information.
- We inspect the aptitude of our model on (~5000 pts/m²) MLS data, as well as high-density helicopter ALS data (>1000 pts/m²). We compare the performance of our projection-based models on the ALS data with the results of state-of-the-art point-based 3D models (Taher et al., 2025), which are trained on the same ALS data.
- We release a high-quality seven species dataset of MLS tree segments containing almost 2000 samples (Korkeala et al., 2025). The data is available at [10.5281/zenodo.17639338](https://doi.org/10.5281/zenodo.17639338).

2 Materials and Methods

2.1 Test site

The test site is located in Southern Finland, in Espoonlahti, Espoo (60.148°N, 24.657°E) and is shown in Figure 1. The area contains a wide variety of trees in urban, semi-urban, and natural environments. The urban areas contain some planted trees, such as lindens, oaks, and maples. The sites with more naturally occurring trees consist mainly of pines, spruces, birches, and some aspens. The MLS data used in this study contains eight species: pine (*Pinus Sylvestris*), spruce (*Picea sp.*), birch (*Betula sp.*), maple (*Acer platanoides*), aspen (*Populus tremula*), rowan (*Sorbus sp.*), alder (*Alnus sp.*) and lime (*Tilia sp.*). Alder was not used in the MLS models, as there were too few labelled samples. The ALS data contains nine species: oak (*Quercus robur*) and the eight aforementioned species.

2.2 Measurements

The MLS data was collected using a FARO Orbis laser scanner (FARO Technologies Inc., Lake Mary, Florida, USA). The Faro Orbis is equipped with a Hesai XT32 lidar (Hesai Technology Co., Ltd., Shanghai, China). The measurements were conducted on the 3rd and 11th of June 2024. 19 measurements were made in total, with a single measurement lasting 7–20 minutes. The MLS coverage can be seen in Figure 1. The laser

¹ Available on Zenodo: <https://doi.org/10.5281/zenodo.13255198>

² Available on Zenodo: <https://doi.org/10.5281/zenodo.17077256>

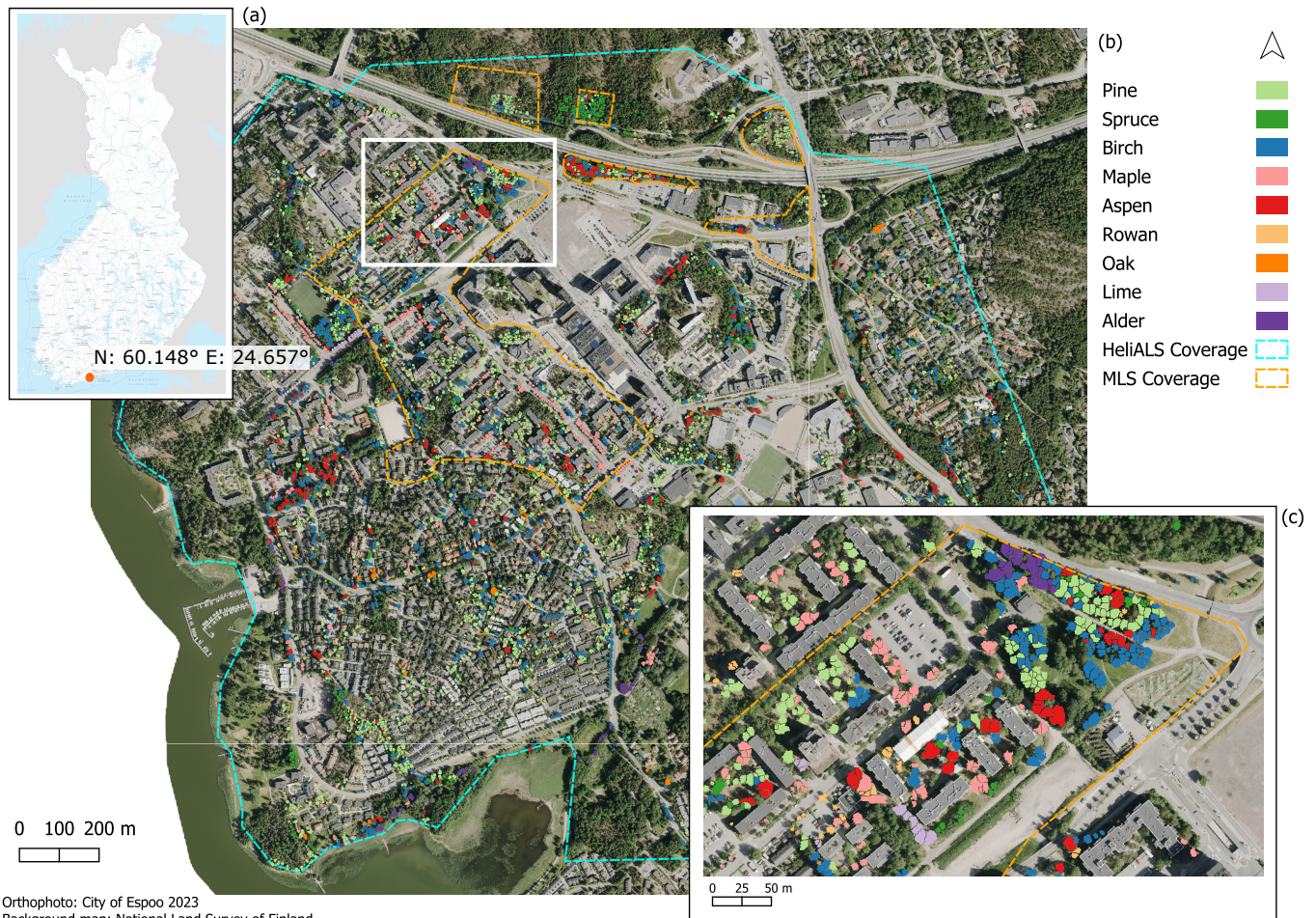


Figure 1: Visualisation of the test site in Espoonlahti. (a): Location of the test site. (b): Orthophoto showing Espoonlahti. The tree segments, as well as the coverage of the different scanning methods, are visible. (c): A zoomed-in view of the orthophoto in (b), showing the tree segments in more detail. Figure adapted from [Taher et al. \(2025\)](#).

scanner was mounted on a backpack. The key scanner properties are presented in Table 1.

The ALS data was gathered in the summer of 2023 by a helicopter equipped with three Riegl (Riegl GmbH, Horn, Austria) laser scanners: VUX-1HA, miniVUX-1DL, and VQ-840-G. The different scanners operate on different wavelengths, see Table 1. The flight altitude of the helicopter was approximately 100 m. Further information on ALS data collection is available in [Taher et al. \(2025\)](#).

Table 1: Scanner Properties.

Property	ALS			MLS
	VUX-1HA	miniVUX-1DL	VQ-840-G1	Hesai XT32
Divergence $V \times H$ (mrad)	0.5	0.5×1.6	1	0.7×1.7
Pulse Repetition Rate (KHz)	1017	100	200	20
Range (m at N% reflectivity)	85 (10%)	140 (20%)	150 (20%)	80 (10%)
Wavelength (nm)	1550	905	532	905
Beam diameter at ground ^a (mm)	50	50×160	100	7×17

^a At a 100 m (ALS) and 10 m (MLS) range from scanners.

2.3 Data preprocessing

The preprocessing of the ALS data was conducted on RiProcess (Riegl) and TerraScan (Terrasolid Ltd., Helsinki, Finland) software. Importantly, the data used in this study contains intensity information from each of the three channels for each point. This was achieved by using nearest-neighbour interpolation to fill in missing intensity values. Reflectance was used as the "source" for the intensity in RiProcess, i.e. the intensity values were distance-adjusted. The trees were segmented using a watershed segmentation-based algorithm introduced first in [Yu et al. \(2010\)](#) and tested in [Kaartinen et al. \(2012\)](#), and called Local Maxima Finding (FGI_LOCM). The field reference was collected using a browser-based solution by the employees of the Finnish Geospatial Research Institute (FGI). For further information on data processing and reference data collection, we refer the reader to [Taher et al. \(2025\)](#).

The raw MLS data from the scanner was first processed by the FARO Connect software, which applies Faro's 3D SLAM algorithm. The point clouds were then randomly subsampled to a spatial resolution of 2 cm, where the minimum distance between any two points is at least 2 cm. Noisy points were re-

Table 2: Species distribution and model training splits for the different data acquisition methods.

Species	Data type					
	ALS			MLS		
	Train	Test	Total	Train	Test	Total
<i>Majority species</i>						
Pine (<i>Pinus Sylvestris</i>)	1863	465	2329	639	116	755
Spruce (<i>Picea</i> sp.)	537	134	671	248	62	310
Birch (<i>Betula</i> sp.)	1225	307	1531	309	65	374
Maple (<i>Acer platanoides</i>)	543	136	676	188	46	234
<i>Minority species</i>						
Aspen (<i>Populus tremula</i>)	377	94	472	87	21	108
Rowan (<i>Sorbus</i> sp.)	163	41	204	48	9	57
Oak (<i>Quercus robur</i>)	53	13	66	-	-	-
Lime (<i>Tilia</i> sp.)	127	32	158	52	14	66
Alder (<i>Alnus</i> sp.)	104	27	131	-	-	11 ^a
Total	4989	1249	6238	1582	333	1904

^a Not used in MLS models.

moved using a Statistical Outlier Removal -filter (SOR filter). The SOR filter evaluates the average distances to k neighbours for each point and removes points for which the average distance is greater than the average distance of all points plus n times the standard deviation of the average distances. Then, a Cloth Simulation Filter (Zhang et al., 2016) was applied to the point cloud, to identify the ground points. The measurement sites contained urban elements, such as buildings, cars, and traffic signs, which were manually removed from the point clouds. At this stage, the point clouds contained only the trees. The preprocessing steps were performed using open source CloudCompare software (CloudCompare development team, 2024).

Individual tree segmentation of the MLS trees was done with the TreeIso algorithm (Xi and Hopkinson, 2022), which is based on a cut-pursuit algorithm for weighted graphs (Landrieu and Obozinski, 2017). The segments produced by TreeIso were manually checked, and unsatisfactory segments were manually corrected using CloudCompare.

To compare the segmented MLS trees with the reference data, they need to be transformed from the local coordinates of the scanner to the global ETRS-TM35FIN coordinate system. To achieve this, we calculated a rigid transformation between the coordinates of each MLS-scan, x_{local} , and global ALS coordinates based on anchor points, such as traffic signs, that were found in both point clouds. We calculated an optimal transformation $x_{\text{global}} = Rx_{\text{local}} + t$, where R is a rotation matrix, t a translation vector, and x_{global} the new transformed coordinates, that minimised the squared distance between the ALS and MLS anchor points.

After transforming the points to the global coordinates, segmented trees were matched with the reference data. We adopted the same strategy as in Hakula et al. (2023), and utilised a Hausdorff distance based closest neighbour algorithm, as presented in Yu et al. (2006). Two points (trees), $a \in A$ and $b \in B$, in different sets (measurement data and reference data), A and B , were considered a match if a is the closest point to b in A , and b is the closest point to a in B . In addition, the distance between the matched points was required to be less than 3 m for them to be considered a match. The reference data for the MLS data is

the same as for the ALS data.

In total, we arrive at 1915 MLS segments and 6238 ALS segments. The species-wise distributions in the data can be seen in Table 2. The difference between the data from the different acquisition methods is visualised in Figure 2, where the left tree (MLS) has a much higher point density, and especially the trunk and branch structure is clearer. The tree on the right (ALS) on the other hand has comparable, or even more refined, canopy structure, due to it being scanned from above, as opposed to the MLS scans. In the MLS data, there are some trees which were captured by multiple different measurements due to overlapping measurement paths. As distinct scans are inherently different, and hence contain useful unique data, we included all viable scans of such trees in the dataset. However, to avoid bias in the model testing, we ensured that all such trees belong to the training set and that the models were not tested on such trees.

2.4 Methodology

From each tree point cloud, we created projection images by three distinct methods: (1): an orthographic projection with intensity values as colours (OP), (2): an orthographic projection with RGB-colours coming from normal vector estimations, NormalView (NV), and (3): an orthographic projection where each pixel is either black or white (WOP), which is in essence a silhouette image. Further explanations of the colouring schemes are in Section 2.4.1. The models trained on WOP-images serve as a baseline, to see how well the trees can be classified with only projection images, without any radiometric input. With the projected images, we trained a classification model that takes images as input. To this end, we used the YOLO³ architecture, as provided by Ultralytics (Ultralytics Inc. Frederick, Maryland, USA) (Jocher et al., 2023).

From the MLS data, we create images according to the three methods mentioned above. From the ALS data we create two image datasets: one with images from seven species to compare the models trained on ALS data more directly with the models trained on MLS data, and the other with images from

³<https://github.com/ultralytics/ultralytics>



Figure 2: The same pine tree as captured by (a) the backpack mobile scanner, and (b) helicopter-ALS. The point counts of the segments are 399 239 and 94 586 respectively. The colouring of the points is purely for visualisation purposes.

the full dataset with nine species, to compare our models with the benchmark in [Taher et al. \(2025\)](#). Both ALS datasets contain images created by the three methods mentioned above. We analyse the viability of the image creation approaches separately for both the seven and nine species datasets.

2.4.1 Image creation

For all colouring schemes, the orthographic projection images are created by projecting the 3D points of the tree onto a projection plane. The pixel coordinates are obtained by finding the orthogonal, or perpendicular, projection of the point onto the plane. The projection plane is the xz -plane, and hence the projection corresponds to extracting the x - and z -coordinates of the points. The projections are taken from multiple angles, as the silhouette of the tree varies depending on the viewing an-

gle. The projections from different angles are achieved by rotating the point cloud around the z -axis and projecting onto the xz -plane. In this study, we used five different viewpoints, corresponding to rotations of 0° , 72° , 144° , 216° or 288° around the z -axis.

From each angle, we created two images: the full projection containing all points and a sliced image to gain insight of the structure of the tree closer to the trunk. This information can be the growing direction of branches, for example. To generate the sliced images, we excluded all points in the rotated point cloud whose y -coordinate satisfied $y > t_y + k$, where t_y is the estimated y -coordinate of the tree trunk, and k is a used-defined threshold. The remaining points were used to create the image. In this study, we used $k = 0.7$ m. This selection provides useful structural information of the insides of the tree, while be-

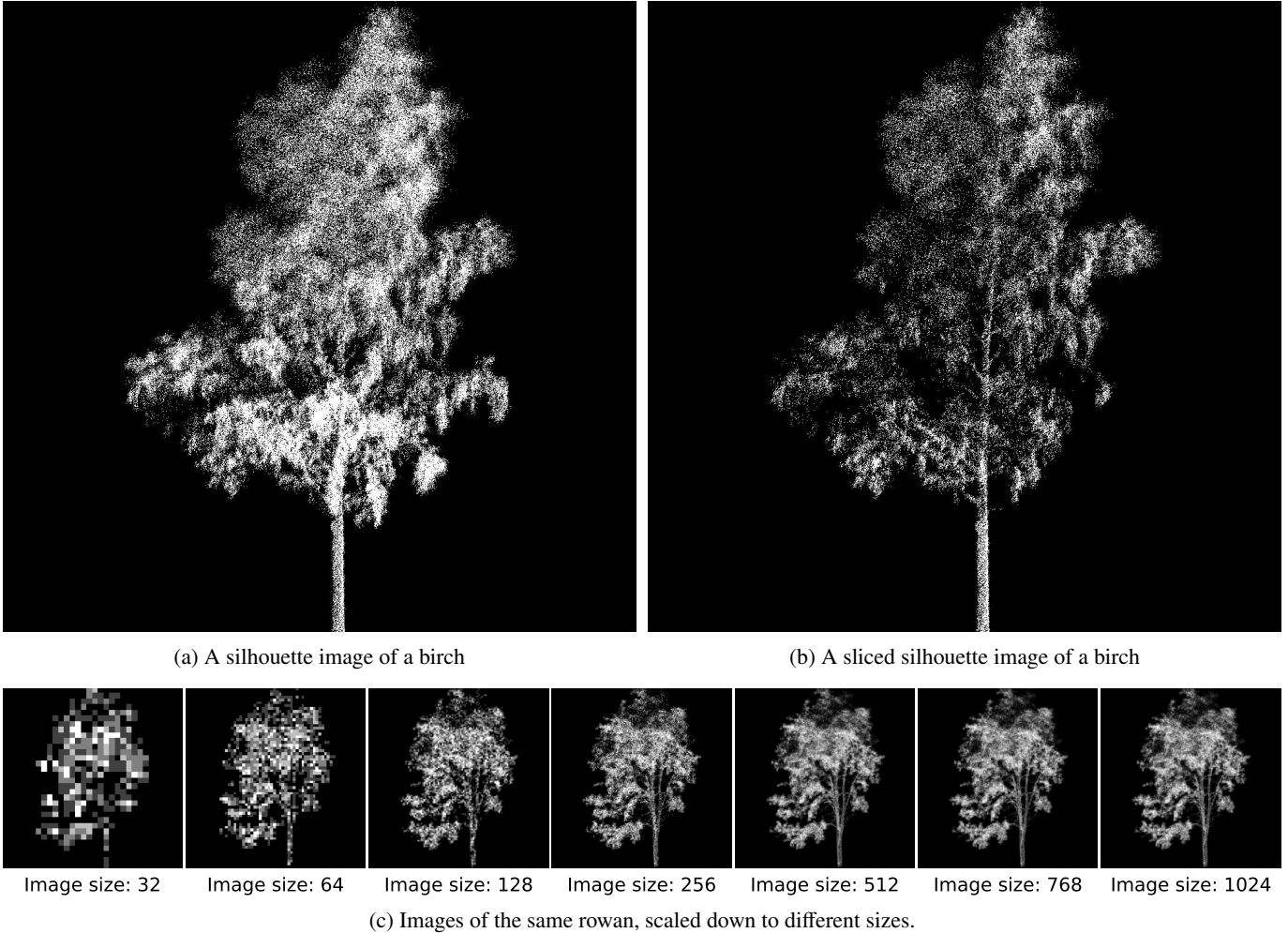


Figure 3: (a)-(b) Two examples of images used in training the models. The images are WOP images created from the same birch from the same angle. (a) All the points are used for the projection. (b) Points nearest to the "viewing plane" are removed to reduce occlusion on the trunk and inner branches. (c) Images in different resolutions of the same rowan. The resolution is achieved by bilinearly interpolating the image of size 1024×1024 .

ing robust against errors in the trunk position estimation. The differences between the full images and the sliced images can be seen in Figures 3a and 3b. Notably, the trunk and inner branches are more visible in the sliced image than in the full image. Consequently, we created ten 512×512 images of each tree per colouring scheme, which are discussed below. In addition, to test the effect of image size on classification accuracy, we created images of size 1024×1024 from the MLS data.

In the OP images, we used the intensity values of the points as a single-channel colour input. The intensity values belong to the interval $[0, 65\,536]$ and were normalised by dividing by the maximum value, $65\,536$, since the absolute scale of the intensity can reveal relevant information about the tree. The scaled intensity values were then linearly scaled to the interval $[0, 255]$, and rounded to integers. These values were then used as input for each of the three 8-bit colour channels in an RGB-image, resulting in a greyscale image. The ALS data contains information from three intensity channels, from which we created intensity-coloured images by using different permutations of the intensities. We created greyscale intensity images

from each individual channel as described for the MLS data, and also three types of images containing two different channels, and finally images using all three channels. For the images containing two different channels, the third colour value in the images was set to zero. For the images containing data from all three channels, we performed a similar normalisation as above and used the three channels as input to the red, green, and blue colour channels. The various colouring schemes are illustrated in Figure 4.

For NV images, we first estimated a normal vector for each point. The normal at a point is estimated by finding the nearest N points of the point in question and fitting a plane via principal analysis. In this study, we set $N = 20$. The unit-length normal vector of this plane was then chosen as the normal. We oriented the normals to point outward, so that the angle between the normal vector and the vector from the point to the estimated trunk is greater than 90° . Subsequently, the components of the normal vector were used as the red, green, and blue colour channels, after a linear scaling to the interval $[0, 255]$, and rounding to integer values.

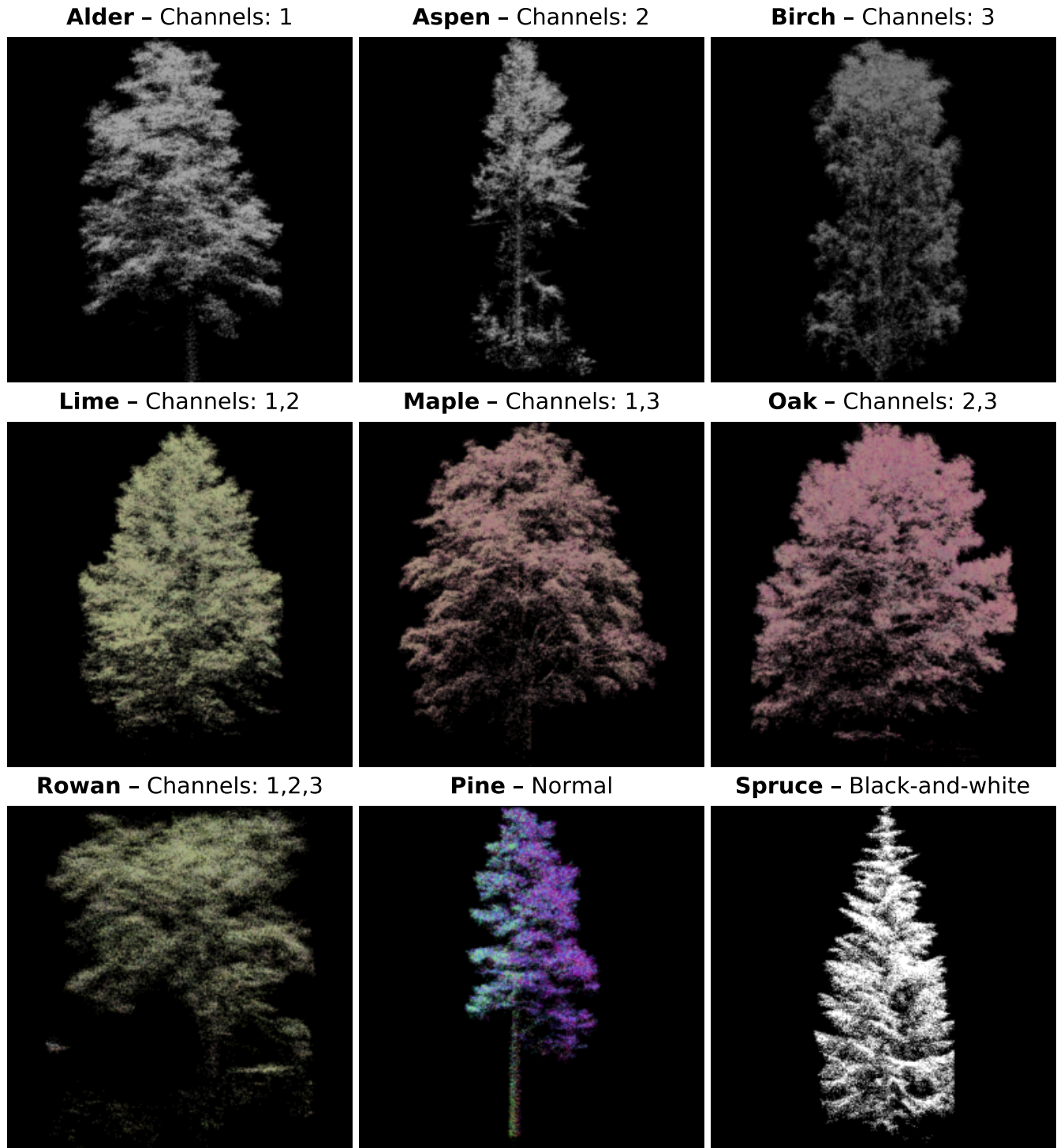


Figure 4: Example images of the nine different tree species and image colouring methods used in model training. All samples are captured by HeliALS. For explanations for the colours, see section 2.4.1.

In the WOP images, a pixel was simply coloured white, if there is a projected point corresponding to it. For the intensity and normal images, we applied a Gaussian convolution kernel, to make the images smoother. The convolution kernel is 3×3 with a standard deviation of 0.85. No filter was applied to the

WOP images.

Projecting the points onto a two-dimensional plane inherently causes information loss, as we lose one degree of spatial freedom. Consequently, we lose intrinsic structural relationships in the data. The projection tactics described in this section at-

tempt to combat this: multiple viewing angles provide a more thorough view of the tree than one singular angle, and the slice images allow the models to see "inside" the trees, as can be seen in Figure 3. The key idea behind the normal projections is to embed three-dimensional structural information into the images via colour. Normal vectors describe the local three-dimensional geometry of each point. Another way this could be achieved is by using eigenfeatures derived from the local structural tensor of each point, as is done by Blackburn et al. (2025).

Additionally, we examined the effect of image size in model training on model performance. Image size refers to the parameter passed on to the YOLO model in the training phase. The input images are scaled to the set image size by applying bilinear interpolation. All images were created to have size 1024×1024 , and were scaled using the bilinear interpolation to the set size when training the model. Ultralytics implements the scaling using OpenCV’s `resize`-function (Bradski, 2000). We tested the effect of image size only on the intensity-coloured images. The differences in perceived visual quality are large for the smaller image sizes, as demonstrated by Figure 3c. We see that a significant portion of visual details are lost in images sized 128×128 and smaller. However, the visual differences are not as prevalent between the larger images.

2.4.2 Model training

As the classification model, we used the YOLOv11x architecture, provided by Ultralytics (Jocher et al., 2023). The model is pretrained on the ImageNet dataset (Deng et al., 2009). The training parameters can be seen from Table 3. We divided the data so that approximately 80% of the data is used for model training, and 20% is used for testing.

In the training phase, we used early stopping to prevent overfitting and to save time. Early stopping means stopping training prior to reaching the set number of epochs, if no improvement in validation metrics is observed for a certain number of epochs. Ultralytics provides this functionality via the `patience` parameter, which was set to 30. Inference is done by creating images from 25 different angles, and aggregating the results to arrive at the final prediction, which is the species with the highest aggregated probability. For each angle, we create the full and sliced images, so 50 images in total are used to predict the species. This method of inference adds a significant degree of robustness to the prediction, at the cost of computational time.

Image augmentations in the training phase of image classification models are recognised to be of significant benefit to model robustness and to avoid overfitting (Shorten and Khoshgoftaar, 2019). The augmentations can include geometric transformations (translations, scaling, and horizontal flips), colour transformations (hue, saturation, and brightness adjustments), blocking parts of the image, and combining multiple images into one. We used `RandAugment` (Cubuk et al., 2020), as the image augmentation policy. The implementation is embedded into YOLOv11 by Ultralytics, and their implementation relies on the implementation by PyTorch⁴.

The models were trained on a laptop with 32 GB of RAM and a 12 GB NVIDIA RTX A3000 GPU. Python version 3.11. was

⁴<https://docs.pytorch.org/vision/main/generated/torchvision.transforms.RandAugment.html>. Visited on 27.08.2025.

Table 3: Parameters used in model training. If a parameter has multiple values, the first one refers to ALS models, and the second one to MLS models.

Parameter	Value
Epochs	400
Image size	256 / 512
Batch size	16 / 5
Optimizer	AdamW
lr0 ^a	0.0005
Dropout	0.15
Patience ^b	30
Momentum ^c	0.8
Learning rate scheduler	Cosine
Augmentation policy	RandAugment

^a Initial learning rate.

^b Number of epochs to wait before stopping training early if performance does not improve.

^c β_1 parameter in AdamW; controls incorporation of past gradients.

used for the image creation and model training, with PyTorch version 2.7.0. and CUDA 12.4. As an exception, when testing the effect of image size on model performance, the models using image sizes 768 and 1024 were trained on a desktop computer with 256 GB of RAM and a 24 GB Nvidia Quatro RTX A6000 GPU, due to high VRAM consumption.

2.5 Model evaluation

To evaluate the trained models, we utilised four macro-level metrics: overall accuracy (OA), macro-average accuracy (MAA), macro-average F_1 -score (MAF_1), Cohen’s kappa (K) (Cohen, 1960) and three species-level metrics: precision (P), recall (R) and species-wise F_1 ($F_{1,s}$). We denote true positives TP_s , true negatives TN_s , false negatives FN_s , and false positives FP_s , where s denotes the species.

Overall accuracy is defined as the ratio of correct predictions over all test samples

$$OA = \frac{1}{N_{test}} \sum_{i=1}^{N_{test}} \mathbb{1}(\hat{y}_i = y_i),$$

where N_{test} is the number of samples in the test set, $\mathbb{1}$ is the indicator function, \hat{y}_i is the predicted label of the i th segment, and y_i is the correct label of the i th segment. OA is a straightforward metric for classification models, but can be a poor indicator of performance, for example if the underlying class distribution is imbalanced (He and Garcia, 2009).

The species-wise precision, recall, and F_1 -score are defined as

$$P_s = \frac{TP_s}{TP_s + FP_s}, \quad R_s = \frac{TP_s}{TP_s + FN_s}, \quad F_{1,s} = \frac{2P_sR_s}{P_s + R_s}$$

To gain insight of model performance in the presence of the aforementioned imbalance in the species distribution, we also calculated the macro-average accuracy for each model. MAA is more sensitive to model behaviour on the minority species than OA, as each species has equal weight. In addition, we

evaluated the macro-average F_1 -score. The MAA is defined as the arithmetic mean of species-wise recalls, while the MAF_1 is defined as the arithmetic mean of species-wise F_1 scores.

$$MAA = \frac{1}{|S|} \sum_{s \in S} R_s, \quad MAF_1 = \frac{1}{|S|} \sum_{s \in S} F_{1,s}$$

where S denotes the set of all species in the dataset and $|S|$ the number of species in the set. The Kappa score is defined as

$$K = \frac{p_o - p_e}{1 - p_e},$$

where p_o is the empirical agreement observed between the predictions and the ground truth and p_e is the proportion of samples agreed upon if the predictions were given by chance.

3 Results and Discussion

In this section, we evaluate the performance of models and provide an analysis of the results. In Section 3.1, we show the performance of the models trained on MLS data and seven species, and on ALS data, both with seven and nine species. Section 3.2 presents our analysis of the effect of image size on model performance.

3.1 Model performance evaluation

The macro-level model performance metrics for the models trained on MLS data are presented in Table 4, and the results for the ALS models are visible in Table 5, for both seven and nine species. The species-level metrics are visible in Figures 5 and 6, for the MLS and ALS models respectively. In the following, Channel 1 refers to intensity information provided by VUX-1HA, Channel 2 to miniVUX-1DL, and Channel 3 to VQ-840-G.

NormalView demonstrates the strongest performance on the MLS data, as can be seen in Table 4. It achieves the best macro-level performance metrics across the board. The strong results in MAA and MAF_1 highlight the ability of NormalView to take into account even minority species in dense MLS data. This observation is supported by the species-wise performance presented in Figure 5. NormalView achieves the highest F_1 for all species except for spruce and aspen.

The intensity-based model performs better than the black-and-white model, but the differences in performance are marginal. For the majority species, the species-wise performance is similar across the models. However, as Figure 5 shows, the differences start to show for the minority species. The black-and-white model performs notably worse than the other two models on rowan and lime.

The overall metrics for species classification for the ALS data are slightly lower than on the MLS data, as illustrated in Table 5. This can likely be attributed to the higher point density and superior segment quality in the MLS data. The results on the seven species ALS data remain strong, however, with the OA (MAA) being 92.6% (88.3%) or higher for each model. The average F_1 -scores and Cohen’s kappas all also exceed 90%, except for the macro- F_1 scores for the normal model, and the models using intensity channels 1 and 3, and

2 and 3. On all the models, the MAA is noticeably lower than OA.

On the nine species dataset, the OAs (MAAs) are 91.6% (77.9%) or higher for each model. There is more notable separation between the OA and MAA for the models trained on nine species, when compared to the MLS models or models trained on seven species. On nine species, the models using multiple intensity channels perform more consistently than the others.

Overall on the ALS data, the best performing model is the one using all three intensity channels, achieving an OA (MAA) of 93.6% (90.6%) on seven species, and 92.5% (84.9%) on nine species. On seven species it is followed closely by the model using only intensity channel 1, which achieved similar performance in all other macro-level metrics, except having an MAA of 90.1%, which is the second highest of the models. On nine species, the second best performer is the model using intensity channels 1 and 3. The overall accuracies of all models are within a percentage point for seven species, and within 1.3 percentage points for nine species. There is a bit more separation in the MAA and MAF_1 metrics, which imply that there are more noticeable differences in how different models are able to account for minority species.

The difficulty of predicting minority species can be seen in Figure 6: the metrics are lower for aspen, rowan, and lime, and especially for oak and alder. On the majority species, especially on pine and birch, the species-wise metrics are extremely strong. The model using all intensity channels has the most balanced performance across species. The models using two intensity channels perform extremely similarly on both the seven species and nine species datasets, and on the nine species dataset they outperform the single-channel and geometry-based models. This, and especially the adeptness of the three-channel model, indicate that multispectral information is beneficial on datasets with numerous species.

With the seven species dataset, NormalView and the black-and-white model perform comparatively with all the other models, with the MAAs losing out by less than two percentage points compared to the best model. On nine species, they are notably outperformed by the models using multiple intensity channels. Their performance is on an equal footing with the models using a single intensity channel. Their macro-level metrics are substantially worse than those of the three-channel model. However, the OAs (MAAs) of NormalView and the black-and-white model, 91.8% (79.1%) and 91.6% (79.5%) respectively, indicate strong performance, only slightly losing out to the best model (FGI-PointTransformer-DL-3D) in Taher et al. (2025), which is trained on the same data, and uses full radiometric information.

3.2 Effect of image size on model performance

Figure 7a shows that increasing image size improves model performance to a certain extent. The highest OA (95.2%) and MAA (93.8%) are achieved by the model using 512 as the image size. The models using higher image size, 768 and 1024, perform slightly worse than the model using size 512, and rather equally to the model using size 256. The training accuracies are markedly higher than test accuracies for all models. Curiously, the model using size 512 has the third-worst train-

Table 4: Performance metrics of models trained on MLS data. Bolded values indicate the best performance in each metric.

Type	OA (%)	MAA (%)	MAF ₁ (%)	K (%)
Intensity	94.6	91.6	91.7	93.1
Normal	95.5	94.8	93.1	94.2
Black-and-white	94.0	90.7	89.8	92.3

Table 5: Comparison of model performance metrics on ALS data for 7 and 9 species. Bolded values indicate the best performance in each metric respectively for 7 and 9 species. Channel 1 refers to intensity information provided by VUX-1HA, Channel 2 to miniVUX-1DL, and Channel 3 to VQ-840-G.

Type	7 Species				9 Species			
	OA (%)	MAA (%)	MAF ₁ (%)	K (%)	OA (%)	MAA (%)	MAF ₁ (%)	K (%)
Channels: 1	93.6	90.1	91.1	91.5	91.8	79.7	82.4	89.2
Channels: 2	93.2	89.5	90.5	91.0	92.2	80.3	83.1	89.8
Channels: 3	93.4	89.5	90.3	91.2	91.2	77.9	80.8	88.5
Channels: 12	93.1	89.6	90.5	90.9	91.8	83.2	85.4	89.3
Channels: 13	93.1	88.8	89.9	90.8	92.3	84.2	85.3	90.0
Channels: 23	93.2	88.3	89.4	91.0	92.1	82.3	83.6	89.6
Channels: 123	93.6	90.6	91.1	91.5	92.5	84.9	86.8	90.2
Normal	93.4	88.9	89.9	91.2	91.8	79.1	81.8	89.2
Black-and-white	93.5	89.5	90.5	91.3	91.6	79.5	82.9	89.0

ing accuracy, surpassing only the models using sizes 32 and 64. This hints that the model overfitted to the training data the least among the models. The model using image size 512 achieves better results than the model trained on intensity-based images, where the initial image size is set to 512, which are visible in Table 4. Computationally, the models using larger image sizes require more memory and processing power, both during training and inference.

Figure 7b shows that the images created into size 1024×1024 tend to have more empty pixels. The pixel sizes are 1.64 cm (± 0.47 cm), and 3.28 cm (± 0.93 cm) for the sizes 1024 and 512, respectively, when evaluated by the average heights of the trees.

3.3 Further discussion

The results in section 3.1, as well as Figure A.1, indicate that NormalView is highly adept at classifying tree species from high-density MLS data. Especially the confusion matrices A.1 show that NormalView takes minority species, rowan and lime, into account better than intensity-based models, or models using black-and-white images. Compared to the model trained on black-and-white images, NormalView achieved a 4.1 percentage points better MAA and 3.3 percentage points better MAF₁, see Table 4. This implies that if we only have geometric data on hand, the normal vector colouring improves classification performance.

On the full ALS dataset, models using multiple intensity channels proved to be the best. The model with all three intensity channels was a strong performer with the seven species and the nine species datasets. This is in accordance with the findings in Taher et al. (2025), where they found that especially low-density point cloud data benefits from multispectral informa-

tion. On lower-density data, the importance of radiometric information becomes more significant, as the data is sparser, and the underlying geometry of the point cloud becomes inconsistent and more unreliable. The performance of the best models on the data is comparable to the best models of the benchmark conducted by Taher et al. (2025), where they achieved an OA (MAA) of 92.0 % (85.1 %) on a similar train-test split as here. Our best-performing model, the one with all three intensity channels, shows essentially equal performance. The corresponding metrics for NormalView are 91.8 % (79.1 %), which are worse, but not by a large margin. The key difference is that the best model in the benchmark utilised full radiometric data from all three scanners, while NormalView uses only geometric information. Images coloured by the normal vector estimations benefit from the tree point clouds having consistent and high-density trunks and branches, as this allows for consistent colour gradients. This likely explains the comparatively stronger performance of NormalView on MLS data, compared to ALS data. On the ALS dataset with the same seven species as in the MLS data, NormalView was not the strongest performer, unlike on the MLS data. The results on the MLS data suggest that especially in applications requiring high-density point clouds, such as exact inventory of natural forests, normal vector colouring provides benefits.

There seems to be little performance difference between the models using ALS data and intensity information from a single channel. On the seven species, the model using channel 1 (VUX-1HA) was the best performer amongst the single channel models, while on nine species the model using channel 2 (miniVUX-1DL) achieved the strongest results. Overall, the performance results are similar and there seems to be little difference in which scanner is used. This suggests that using radiometric information with projection-based methods can be made viable on scanners with varying properties, such as the

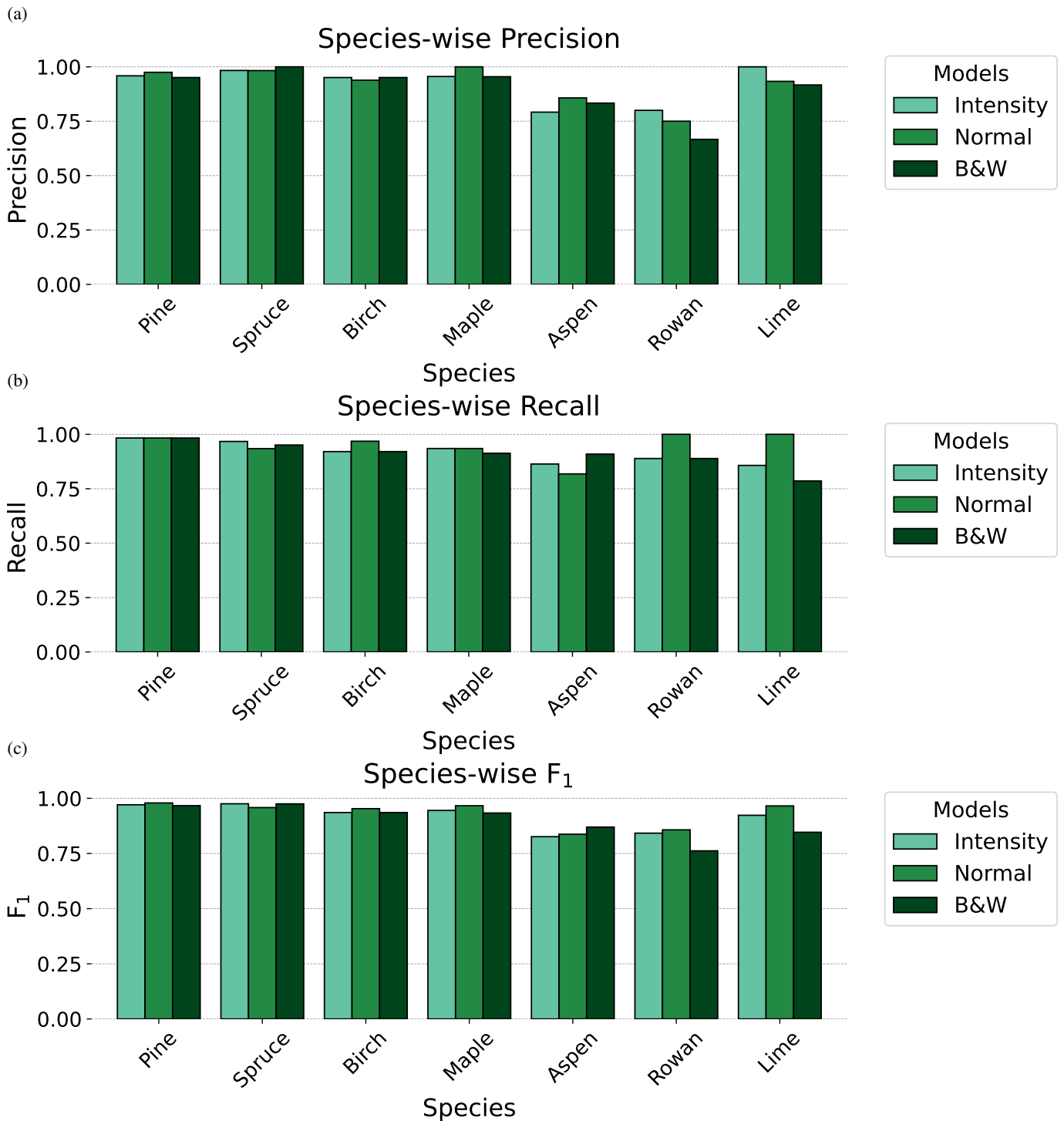


Figure 5: Species-wise metrics of the models trained on MLS data. (a) Species-wise precision, (b) species-wise recall, (c) species-wise F₁ scores. B&W refers to the model trained on black-and-white images.

wavelength of the laser pulse.

We see from Figure 6 that across the board the models perform the worst, by precision and F₁, on oak, and, to a lesser degree, alder. These species are the two with the smallest representation in our dataset, and hence the least variety. In addition, the

segments of the alders and oaks have some impurities, as suggested by Figure 5 in [Taher et al. \(2025\)](#). Alders tend to grow in groups, making segmentation more difficult. A significant portion of oak segments are only partial segments of the trees. The low performance on these species can probably at least partially be attributed to low sample counts and lower-quality seg-

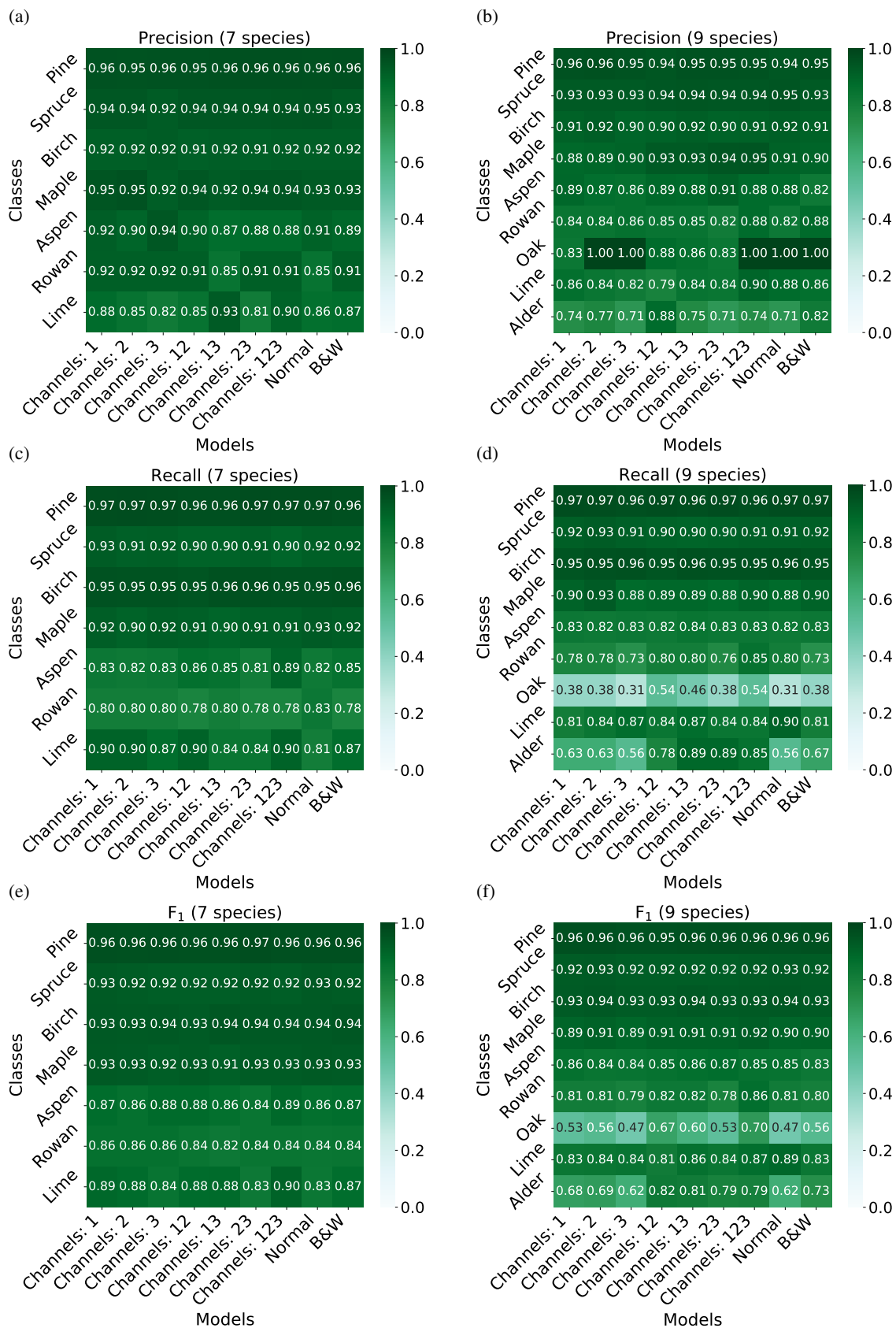


Figure 6: Species-wise precision, recall, and F₁-scores for models trained on ALS data with 7 (left) and 9 (right) species: (a)–(b) precision, (c)–(d) recall, (e)–(f) F₁-scores.

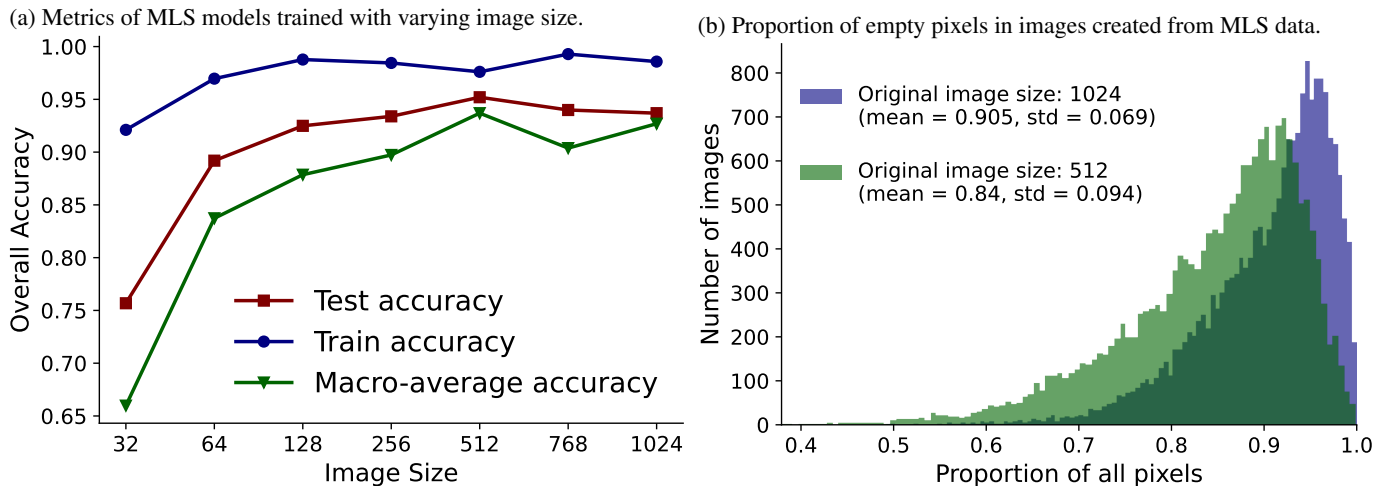


Figure 7: (a) Performance metrics of models trained on MLS data and varying image sizes. (b) Proportions of empty pixels in images created from MLS data to sizes 1024×1024 and 512×512 .

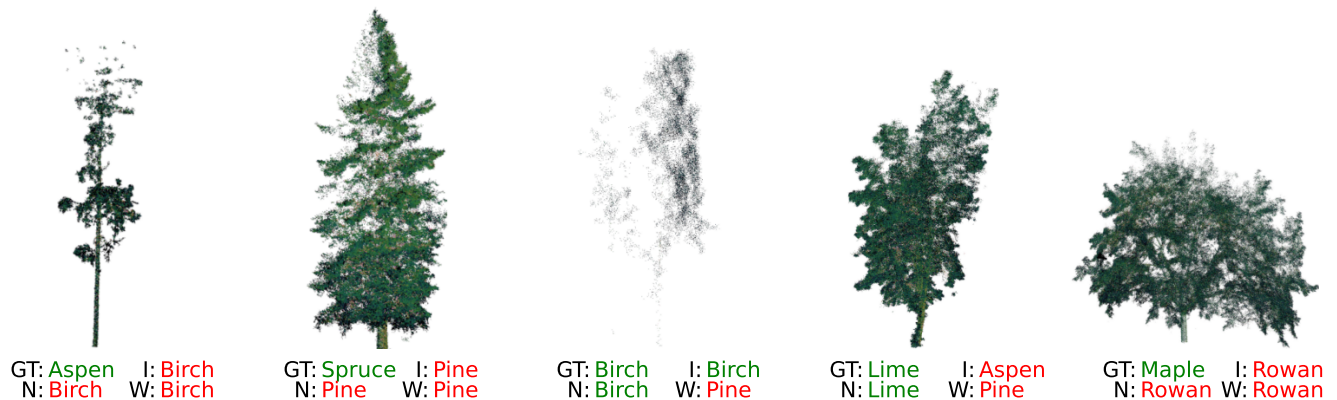


Figure 8: Examples of MLS trees misclassified by at least one model. GT refers to ground truth, I, N and W refer to the predictions given by the intensity, normal and black-and-white models respectively. Green indicates a correct prediction and red an incorrect one.

ments. From the confusion matrices in [A](#) we see that almost all models tend to systematically classify aspens as birches. Birches and aspens have rather similar silhouettes, which explains the errors. Similarly, rowans seem to get classified as maples and birches. Some examples of trees misclassified by the MLS models are shown in [Figure 8](#). It seems that poorly captured trees with lacklustre silhouettes are prone to misclassification, such as the aspen and birch trees in [Figure 8](#). This is not the only explanation for misclassification, as for example the spruce, lime, and maple trees in [Figure 8](#) are captured well by the scanner, and have full silhouettes. To enhance the performance of the models on species with similar silhouettes, one could, for example, include more detailed bark information, as is done in the DetailView method discussed by [Puliti et al. \(2025b\)](#).

The F_1 -scores for aspens are satisfactory across all data modalities and models. On the MLS data, the scores are around 80%, while between 83 and 87% for the ALS data and all nine species. This shows that we are able to map aspens with high

confidence from both MLS and ALS data. The use of multi-spectral information improves the scores by a small margin, but the sensor agnostic NormalView and black-and-white models achieve F_1 scores of 85% and 83% respectively, highlighting the capabilities of projection-based methods.

The black-and-white model is the worst performing model on MLS data, and among the worst performers on ALS data. On the MLS data and the nine species ALS data, it achieves an OA (MAA) of 94.0% (90.7%) and 91.6% (79.5%) respectively. These results show that even using purely black-and-white orthographic projections allows us to classify tree species on a reasonably high level. The performance is due to the high capabilities in which modern image-based architectures, such as YOLO, are able to extract meaningful representations and features from the data. The image classification backbones used in previous studies of tree species classification seem to be, in general, slightly outdated, such as the VGG-11 ([Simonyan and Zisserman, 2015](#)) used by [Marinelli et al. \(2022\)](#), or the DenseNet-201 ([Iandola et al., 2014](#)) used by the DetailView

method in [Puliti et al. \(2025b\)](#).

As seen in Section 3.2, using an appropriate image size can significantly improve the predictive power of the networks. Using larger images allows for more detailed information, at the cost of longer training times and higher hardware requirements. Hence, it is critical that before training the models, we have some notion of the appropriate size into which to create the images. For images created into size 1024×1024 , one pixel size corresponds approximately to a square of size $1.64 \text{ cm} \times 1.64 \text{ cm}$ in the projective plane. In the preprocessing phase, we subsampled the point clouds to a spatial resolution of 2 cm, which is larger than the size of the pixels. As a result, there are many empty pixels, even at points where we would assume the tree to be visible. Certainly, as a general guideline, the resolution should be such that one pixel encompasses an area that is slightly larger than the spatial resolution of the underlying point cloud data. This is supported by our findings in Section 3.2, where the model with image size 512 was the best. For images of size 512×512 , the pixel size is $3.28 \text{ cm} \times 3.28 \text{ cm}$, which is roughly one-and-a-half times larger than the spatial resolution of the densest parts of the point clouds. Figure 7b shows that higher resolution images tend to have more empty pixels, which is, of course, expected. Convolutional neural networks (CNNs) are usually designed with the assumption that the input data will be dense ([Graham et al., 2018](#)). If the image size in the projections is large, the images will start to be rather sparse, in the sense that most of the image will be empty pixels, containing no information. At the very least, this will waste time and require more computational resources with little to no added performance benefit. In the worst case, empty pixels will negatively affect the model.

3.4 Limitations

The datasets used in this study, while containing the most predominant boreal tree species, are incomplete even for traditional Finnish ecosystems. Hence it is not applicable to use the models directly in practice. The training of the models also requires significant amounts of annotated data. Collecting and labelling training data for deep learning models is notoriously time-consuming and, as such, highlights the need for large multispecies datasets, such as the recently released FOR-species20k and the MS-ALS-SPECIES dataset ([Puliti et al., 2025a](#); [Hyypä et al., 2025](#)).

In the MLS data, the segment quality is extremely high. Our empirical experience is that better segment quality improves classification performance. For real world applications, the segment quality might be significantly lower, and the accuracy of the models may suffer from these inaccuracies. The effect of segment quality on tree species classification warrants further study.

4 Conclusions

In this study, we presented a sensor-agnostic projection-based method, NormalView, for tree species classification purposes. The method embeds local geometric information of tree point clouds into projection images via colour. The colour values are derived from normal vector estimates of the points.

We compared our projection-based method with models trained on projection images using intensity information and models using black-and-white projection images. We found that on high-density seven species MLS data our NormalView achieves superior performance compared to the other methods, with the overall accuracy (macro-average accuracy) reaching 95.5 % (94.8 %). For high-density helicopter ALS data, we found that our method achieves comparable performance with methods using intensity information. However, the best model on the ALS data was the one using intensity information from three channels of the multispectral ALS. It achieved an overall (macro-average) accuracy of 92.5 % (84.9 %) on the full dataset with nine species. These results are on par with the best models in [Taher et al. \(2025\)](#), showing that projection-based methods using strong CNN-backbones can achieve performance comparable to that of state-of-the-art 3D models.

Our tests show that using multispectral data, i.e. combining radiometric information from multiple scanners, improves the prediction ability of projection-based models. The benefits are best seen for species belonging to minority classes. We also inspected the effect of image size on model performance, and found that using larger images is beneficial up to a certain point, enhancing the accuracy of the model. For the high-density MLS data we found that image size 512×512 produces the best results.

Data availability

The labeled MLS point clouds and model weights are available in ([Korkeala et al., 2025](#)), under Creative Commons Attribution-NonCommercial 4.0 International licence. Commercial rights can be granted separately for collaborating companies by FGI.

CRedit authorship contribution statement

Juho Korkeala: Writing - Original Draft, Conceptualization, Methodology, Software, Investigation, Data Curation, Visualization. **Jesse Muhojoki:** Writing - Original Draft, Resources, Supervision. **Josef Taher:** Writing - Review & Editing, Conceptualization. **Klaara Salolahti:** Writing - Review & Editing, Data Curation, Visualisation. **Matti Hyypä:** Writing - Review & Editing, Data Curation. **Antero Kukko:** Writing - Review & Editing, Project Administration, Funding Acquisition, Supervision. **Juha Hyypä:** Writing - Original Draft, Project Administration, Funding Acquisition, Supervision.

Acknowledgments

The study has received funding from the Research Council of Finland (RCF), and the NextGenerationEU instrument through the following grants "Collecting accurate individual tree information for harvester operation decision making" (RCF 359554), "Digital technologies, risk management solutions and tools for mitigating forest disturbances" (RCF 353264, NextGenerationEU), and "Forest-Human-Machine Interplay - Building Resilience, Redefining Value Networks and Enabling Meaningful Experiences" (RCF 359175) using RCF research Infrastructure "Measuring Spatiotemporal Changes in Forest Ecosystem" (346382)".

Declaration of competing interest

The authors declare that they have no known competing financial interests or personal relationships that could have appeared to influence the work reported in this paper.

References

- Allen, M., Grieve, S., Owen, H., and Lines, E. Tree species classification from complex laser scanning data in mediterranean forests using deep learning. *Methods in Ecology and Evolution*, 14, 09 2022. doi:10.1111/2041-210X.13981.
- Angelstam, P. and Mikusiński, G. Woodpecker assemblages in natural and managed boreal and hemiboreal forest - a review. *Annales Zoologici Fennici*, 31:157–172, 01 1994.
- Blackburn, R. C., Buscaglia, R., Sánchez Meador, A. J., Moore, M. M., Sankey, T., and Sennie, S. E. Eigenfeature-enhanced deep learning: advancing tree species classification in mixed conifer forests with lidar. *Remote Sensing in Ecology and Conservation*, 2025. doi:10.1002/rse2.70014.
- Bradski, G. The OpenCV Library. *Dr. Dobb's Journal of Software Tools*, 2000.
- Breiman, L. Random forests. *Machine learning*, 45(1):5–32, 2001. doi:10.1023/A:1010933404324.
- Chirici, G., McRoberts, R. E., Winter, S., Bertini, R., Brändli, U.-B., Asensio, I. A., Bastrup-Birk, A., Rondeux, J., Barsoum, N., and Marchetti, M. National forest inventory contributions to forest biodiversity monitoring. *Forest Science*, 58(3):257–268, 06 2012. doi:10.5849/forsci.12-003.
- CloudCompare development team. Cloudcompare, version 2.13.1 [software], 2024. URL <http://www.cloudcompare.org/>.
- Cohen, J. A coefficient of agreement for nominal scales. *Educational and Psychological Measurement*, 20(1):37–46, 1960. doi:10.1177/001316446002000104.
- Cortes, C. and Vapnik, V. Support-vector networks. *Machine learning*, 20(3):273–297, 1995. doi:10.1007/BF00994018.
- Cubuk, E. D., Zoph, B., Shlens, J., and Le, Q. V. Randaugment: Practical automated data augmentation with a reduced search space. In *Proceedings of the IEEE/CVF Conference on Computer Vision and Pattern Recognition (CVPR) Workshops*, pages 3008–3017, June 2020. doi:10.48550/arXiv.1909.13719.
- Dalponte, M., Bruzzone, L., and Gianelle, D. Tree species classification in the southern alps based on the fusion of very high geometrical resolution multispectral/hyperspectral images and lidar data. *Remote Sensing of Environment*, 123:258–270, 2012. doi:10.1016/j.rse.2012.03.013.
- Dalponte, M., Ene, L. T., Gobakken, T., Næsset, E., and Gianelle, D. Predicting selected forest stand characteristics with multispectral als data. *Remote Sensing*, 10(4), 2018. doi:10.3390/rs10040586.
- Deng, J., Dong, W., Socher, R., Li, L.-J., Li, K., and Fei-Fei, L. Imagenet: A large-scale hierarchical image database. In *2009 IEEE Conference on Computer Vision and Pattern Recognition*, pages 248–255, 2009. doi:10.1109/CVPR.2009.5206848.
- Gamfeldt, L., Snäll, T., Bagchi, R., Jonsson, M., Gustafsson, L., Kjellander, P., Ruiz-Jaen, M. C., Fröberg, M., Stendahl, J., Philipson, C. D., Mikusiński, G., Andersson, E., Westerlund, B., Andrén, H., Moberg, F., Moen, J., and Bengtsson, J. Higher levels of multiple ecosystem services are found in forests with more tree species. *Nature Communications*, 4(1):1340, Jan 2013. doi:10.1038/ncomms2328.
- Graham, B., Engelcke, M., and Van Der Maaten, L. 3d semantic segmentation with submanifold sparse convolutional networks. In *Proceedings of the IEEE conference on computer vision and pattern recognition*, pages 9224–9232, 2018. doi:10.48550/arXiv.1711.10275.
- Haara, A., Kangas, A., and Tuominen, S. Economic losses caused by tree species proportions and site type errors in forest management planning. *Silva Fennica*, 53(2), 2019. doi:https://doi.org/10.14214/sf.10089.
- Hakula, A., Ruoppa, L., Lehtomäki, M., Yu, X., Kukko, A., Kaartinen, H., Taher, J., Matikainen, L., Hyypä, E., Luoma, V., Holopainen, M., Kankare, V., and Hyypä, J. Individual tree segmentation and species classification using high-density close-range multispectral laser scanning data. *ISPRS Open Journal of Photogrammetry and Remote Sensing*, 9:100039, 2023. doi:10.1016/j.ophoto.2023.100039.
- Hardenbol, A., Kuzmin, A., Korhonen, L., Korpelainen, P., Kumpula, T., Maltamo, M., and Kouki, J. Detection of aspen in conifer-dominated boreal forests with seasonal multispectral drone image point clouds. *Silva Fennica*, 55(4), 2021. doi:10.14214/sf.10515.
- He, H. and Garcia, E. A. Learning from imbalanced data. *IEEE Transactions on Knowledge and Data Engineering*, 21(9):1263–1284, 2009. doi:10.1109/TKDE.2008.239.
- Henrich, J., van Delden, J., Seidel, D., Kneib, T., and Ecker, A. S. Treelearn: A deep learning method for segmenting individual trees from ground-based lidar forest point clouds. *Ecological Informatics*, 84:102888, 2024. doi:10.1016/j.ecoinf.2024.102888.
- Huuskonen, S., Domisch, T., Finér, L., Hantula, J., Hynynen, J., Matala, J., Miina, J., Neuvonen, S., Nevalainen, S., Niemistö, P., Nikula, A., Piri, T., Siitonen, J., Smolander, A., Toneri, T., Uotila, K., and Viiri, H. What is the potential for replacing monocultures with mixed-species stands to enhance ecosystem services in boreal forests in fennoscandia? *Forest Ecology and Management*, 479:118558, 2021. doi:10.1016/j.foreco.2020.118558.
- Hyypä, J. and Inkinen, M. Detecting and estimating attributes for single trees using laser scanner. *The Photogramm. J. Finland*, 16:27–42, 1999.
- Hyypä, J., Yu, X., Ronnholm, P., Kaartinen, H., and Hyypä, H. Factors affecting laser-derived object-oriented forest height growth estimation. *The Photogramm. J. Finland*, 18:16–31, 2003.
- Hyypä, E., Yu, X., Kaartinen, H., Hakala, T., Kukko, A., Vastaranta, M., and Hyypä, J. Comparison of backpack, handheld, under-canopy uav, and above-canopy uav laser scanning for field reference data collection in boreal forests. *Remote Sensing*, 12(20), 2020. doi:10.3390/rs12203327.
- Hyypä, M., Salolahti, K., Hyypä, E., Yu, X., Taher, J., Matikainen, L., Litkey, P., Lehtomäki, M., Hakala, T., Kaartinen, H., Hyypä, J., and Kukko, A. Multispectral airborne laser scanning for species classification in espoonlahti (MS-ALS-SPECIES) [dataset]. Zenodo, 2025. doi: 10.5281/zenodo.17077256.
- Iandola, F. N., Moskevycz, M. W., Karayev, S., Girshick, R. B., Darrell, T., and Keutzer, K. Densenet: Implementing efficient convnet descriptor pyramids. *CoRR*, abs/1404.1869, 2014. doi:10.48550/arXiv.1404.1869.
- Izenman, A. J. Linear discriminant analysis. In *Modern multivariate statistical techniques: regression, classification, and manifold learning*, pages 237–280. Springer, 2013.
- Jocher, G., Qiu, J., and Chaurasia, A. Ultralytics YOLO, Version 8.0.0, Jan. 2023. URL <https://github.com/ultralytics/ultralytics>.
- Kaartinen, H., Hyypä, J., Yu, X., Vastaranta, M., Hyypä, H., Kukko, A., Holopainen, M., Heipke, C., Hirschmugl, M., Morsdorf, F., Næsset, E., Pitkänen, J., Popescu, S., Solberg, S., Wolf, B. M., and Wu, J.-C. An international comparison of individual tree detection and extraction using airborne laser scanning. *Remote Sensing*, 4(4):950–974, 2012. doi:10.3390/rs4040950.
- Kivinen, S., Koivisto, E., Keski-Saari, S., Poikolainen, L., Tanhuanpää, T., Kuzmin, A., Viinikka, A., Heikkinen, R. K., Pykälä, J., Virkkala, R., Vihervaara, P., and Kumpula, T. A keystone species, european aspen (*populus tremula* L.), in boreal forests: Ecological role, knowledge needs and mapping using remote sensing. *Forest Ecology and Management*, 462:118008, 2020. doi:10.1016/j.foreco.2020.118008.
- Koenig, K. and Höfle, B. Full-waveform airborne laser scanning in vegetation studies—a review of point cloud and waveform features for tree species classification. *Forests*, 7(9), 2016. doi:10.3390/f7090198.
- Korkeala, J., Muhojoki, J., Kukko, A., and Hyypä, J. Espoonlahti mobile laser scanning tree species classification (dataset). Zenodo, 2025. doi: 10.5281/zenodo.17639338.
- Kouki, J., Arnold, K., and Martikainen, P. Long-term persistence of aspen – a key host for many threatened species – is endangered in old-growth conservation areas in finland. *Journal for Nature Conservation*, 12(1):41–52, 2004. ISSN 1617-1381. doi:10.1016/j.jnc.2003.08.002.
- Landrieu, L. and Obozinski, G. Cut Pursuit: fast algorithms to learn piecewise constant functions on general weighted graphs. *SIAM Journal on Imaging Sciences*, Vol. 10(No. 4):pp. 1724–1766, 2017. HAL-id: hal-01306779.
- Liang, X., Hyypä, J., Kukko, A., Kaartinen, H., Jaakkola, A., and Yu, X. The use of a mobile laser scanning system for mapping large forest plots. *IEEE Geoscience and Remote Sensing Letters*, 11(9):1504–1508, 2014. doi:10.1109/LGRS.2013.2297418.
- Liu, B., Chen, S., Huang, H., and Tian, X. Tree species classification of backpack laser scanning data using the PointNet++ point cloud deep learning method. *Remote Sens.*, 14(15), 2022a. doi:10.3390/rs14153809.
- Liu, B., Huang, H., Su, Y., Chen, S., Li, Z., Chen, E., and Tian, X. Tree species classification using ground-based lidar data by various point cloud deep learning methods. *Remote Sensing*, 14(22), 2022b. doi:10.3390/rs14225733.
- Liu, B., Huang, H., Tian, X., and Ren, M. Individual tree species classification using the pointwise MLP-based point cloud deep learning method. *Environmental Sciences Proceedings*, 22(1), 2022c. doi:10.3390/IECF2022-13049.
- Liu, M., Han, Z., Chen, Y., Liu, Z., and Han, Y. Tree species classification of lidar data based on 3D deep learning. *Measurement*, 177:109301, 2021. doi:10.1016/j.measurement.2021.109301.
- Ma, X., Qin, C., You, H., Ran, H., and Fu, Y. Rethinking network design and local geometry in point cloud: A simple residual mlp framework, 2022. doi:10.48550/arXiv.2202.07123.
- Marinelli, D., Paris, C., and Bruzzone, L. An approach based on deep learning for tree species classification in lidar data acquired in mixed forest. *IEEE Geoscience and Remote Sensing Letters*, 19:1–5, 2022. doi:10.1109/LGRS.2022.3181680.
- Pauly, M., Keiser, R., Kobbelt, L. P., and Gross, M. Shape modeling with point-sampled geometry. *ACM Trans. Graph.*, 22(3):641–650, July 2003. doi:10.1145/882262.882319.

- Puliti, S., Lines, E., Müllerová, J., Frey, J., Schindler, Z., Straker, A., Allen, M. J., Lukas, W., Rehush, N., Hristova, H., Murray, B., Calders, K., Terryn, L., Coops, N., Höfle, B., Junntila, S., Kruczek, M., Krok, G., Král, K., Levick, S. R., Luck, L., Missarov, A., Mokroš, M., Owen, H., Stereńczak, K., Pitkänen, T., Puletti, N., Saarinen, N., Hopkinson, C., Torresan, C., Tomelleri, E., Weiser, H., and Astrup, R. FOR-species20K [dataset]. Zenodo, 2025a. doi: [10.5281/zenodo.13255198](https://doi.org/10.5281/zenodo.13255198).
- Puliti, S., Lines, E. R., Müllerová, J., Frey, J., Schindler, Z., Straker, A., Allen, M. J., Winiwarter, L., Rehush, N., Hristova, H., Murray, B., Calders, K., Coops, N., Höfle, B., Irwin, L., Junntila, S., Krüček, M., Krok, G., Král, K., Levick, S. R., Luck, L., Missarov, A., Mokroš, M., Owen, H. J. F., Stereńczak, K., Pitkänen, T. P., Puletti, N., Saarinen, N., Hopkinson, C., Terryn, L., Torresan, C., Tomelleri, E., Weiser, H., and Astrup, R. Benchmarking tree species classification from proximally sensed laser scanning data: Introducing the for-species20k dataset. *Methods in Ecology and Evolution*, 16(4):801–818, 2025b. doi:[10.1111/2041-210X.14503](https://doi.org/10.1111/2041-210X.14503).
- Qi, C. R., Su, H., Mo, K., and Guibas, L. J. Pointnet: Deep learning on point sets for 3d classification and segmentation. In *Proceedings of the IEEE conference on computer vision and pattern recognition*, pages 652–660, 2017a. doi:[10.1109/CVPR.2017.16](https://doi.org/10.1109/CVPR.2017.16).
- Qi, C. R., Yi, L., Su, H., and Guibas, L. J. PointNet++: Deep hierarchical feature learning on point sets in a metric space. In Guyon, I., Luxburg, U. V., Bengio, S., Wallach, H., Fergus, R., Vishwanathan, S., and Garnett, R., editors, *Advances in Neural Information Processing Systems*, volume 30, page 5105–5114. Curran Associates, Inc., 2017b.
- Remm, J., Hanski, I. K., Tuominen, S., and Selonen, V. Multilevel landscape utilization of the siberian flying squirrel: Scale effects on species habitat use. *Ecology and Evolution*, 7(20):8303–8315, 2017. doi:[10.1002/ece3.3359](https://doi.org/10.1002/ece3.3359).
- Ruoppa, L., Oinonen, O., Taher, J., Lehtomäki, M., Takhtkeshha, N., Kukko, A., Kaartinen, H., and Hyypää, J. Unsupervised deep learning for semantic segmentation of multispectral lidar forest point clouds. *ISPRS Journal of Photogrammetry and Remote Sensing*, 228:694–722, 2025. doi:[10.1016/j.isprsjprs.2025.07.038](https://doi.org/10.1016/j.isprsjprs.2025.07.038).
- Seidel, D., Annighöfer, P., Thielman, A., Seifert, Q. E., Thauer, J.-H., Glatthorn, J., Ehbrecht, M., Kneib, T., and Ammer, C. Predicting tree species from 3d laser scanning point clouds using deep learning. *Frontiers in Plant Science*, Volume 12 – 2021, 2021. doi:[10.3389/fpls.2021.635440](https://doi.org/10.3389/fpls.2021.635440).
- Serafin, J. and Grisetti, G. Nicp: Dense normal based point cloud registration. In *2015 IEEE/RSJ International Conference on Intelligent Robots and Systems (IROS)*, pages 742–749, 2015. doi:[10.1109/IROS.2015.7353455](https://doi.org/10.1109/IROS.2015.7353455).
- Shorten, C. and Khoshgoftaar, T. M. A survey on image data augmentation for deep learning. *Journal of big data*, 6(1):1–48, 2019. doi:[10.1186/s40537-019-0197-0](https://doi.org/10.1186/s40537-019-0197-0).
- Simonyan, K. and Zisserman, A. Very deep convolutional networks for large-scale image recognition, 2015. doi: [10.48550/arXiv.1409.1556](https://doi.org/10.48550/arXiv.1409.1556).
- Sun, P., Yuan, X., and Li, D. Classification of individual tree species using uav lidar based on transformer. *Forests*, 14(3), 2023. doi: [10.3390/f14030484](https://doi.org/10.3390/f14030484).
- Taher, J., Hyypää, E., Hyypää, M., Salolahti, K., Yu, X., Matikainen, L., Kukko, A., Lehtomäki, M., Kaartinen, H., Thurachen, S., Litkey, P., Luoma, V., Holopainen, M., Kong, G., Fan, H., Rönnholm, P., Polvivaara, A., Junntila, S., Vastaranta, M., Puliti, S., Astrup, R., Kostensalo, J., Myllymäki, M., Kulicki, M., Stereńczak, K., de Paula Pires, R., Valbuena, R., Carbonell-Rivera, J. P., Torralba, J., Chen, Y.-C., Winiwarter, L., Hollaus, M., Mandlbürger, G., Takhtkeshha, N., Remondino, F., Lisiewicz, M., Kraszewski, B., Liang, X., Chen, J., Ahokas, E., Karila, K., Vezeteu, E., Manninen, P., Näsi, R., Hytti, H., Pyykkönen, S., Hu, P., and Hyypää, J. Multi-spectral airborne laser scanning for tree species classification: a benchmark of machine learning and deep learning algorithms, 2025. doi: [10.48550/arXiv.2504.14337](https://doi.org/10.48550/arXiv.2504.14337).
- Tikkanen, O.-P., Martikainen, P., Hyvärinen, E., Junninen, K., and Kouki, J. Red-listed boreal forest species of finland: Associations with forest structure, tree species, and decaying wood. *Annales Zoologici Fennici*, 43, 08 2006.
- Tockner, A., Kraßnitzer, R., Gollob, C., Witzmann, S., Ritter, T., and Nothdurft, A. Tree species classification using intensity patterns from individual tree point clouds. *International Journal of Applied Earth Observation and Geoinformation*, 139:104502, 2025. ISSN 1569-8432. doi:[10.1016/j.jag.2025.104502](https://doi.org/10.1016/j.jag.2025.104502).
- Tran, D., Bourdev, L., Fergus, R., Torresani, L., and Paluri, M. Learning spatiotemporal features with 3d convolutional networks. In *Proceedings of the IEEE international conference on computer vision*, pages 4489–4497, 2015.
- Wang, Y., Sun, Y., Liu, Z., Sarma, S. E., Bronstein, M. M., and Solomon, J. M. Dynamic graph cnn for learning on point clouds. *ACM Trans. Graph.*, 38(5), Oct. 2019. doi:[10.1145/3326362](https://doi.org/10.1145/3326362).
- Wielgosz, M., Puliti, S., Xiang, B., Schindler, K., and Astrup, R. Segmentanytree: A sensor and platform agnostic deep learning model for tree segmentation using laser scanning data. *Remote Sensing of Environment*, 313:114367, 2024. doi:<https://doi.org/10.1016/j.rse.2024.114367>.
- Winberg, O., Pyörälä, J., Yu, X., Kaartinen, H., Kukko, A., Holopainen, M., Holmgren, J., Lehtomäki, M., and Hyypää, J. Branch information extraction from norway spruce using handheld laser scanning point clouds in nordic forests. *ISPRS Open Journal of Photogrammetry and Remote Sensing*, 9:100040, 2023. doi:[10.1016/j.ophoto.2023.100040](https://doi.org/10.1016/j.ophoto.2023.100040).
- Xi, Z. and Hopkinson, C. 3d graph-based individual-tree isolation (treeiso) from terrestrial laser scanning point clouds. *Remote Sensing*, 14(23), 2022. doi:[10.3390/rs14236116](https://doi.org/10.3390/rs14236116).
- Xiang, B., Wielgosz, M., Puliti, S., Král, K., Krüček, M., Missarov, A., and Astrup, R. ForestFormer3D: A Unified Framework for End-to-End Segmentation of Forest LiDAR 3D Point Clouds. In *Proceedings of the IEEE/CVF International Conference on Computer Vision (ICCV)*, pages 24717–24727, 2025.
- Yang, M. and Lee, E. Segmentation of measured point data using a parametric quadric surface approximation. *Computer-Aided Design*, 31(7):449–457, 1999. doi:[10.1016/S0010-4485\(99\)00042-1](https://doi.org/10.1016/S0010-4485(99)00042-1).
- Yu, X., Hyypää, J., Kaartinen, H., and Maltamo, M. Automatic detection of harvested trees and determination of forest growth using airborne laser scanning. *Remote sensing of Environment*, 90(4):451–462, 2004. doi:[10.1016/j.rse.2004.02.001](https://doi.org/10.1016/j.rse.2004.02.001).
- Yu, X., Hyypää, J., Kukko, A., Maltamo, M., and Kaartinen, H. Change detection techniques for canopy height growth measurements using airborne laser scanner data. *Photogrammetric Engineering & Remote Sensing*, 72(12):1339–1348, 2006. ISSN 0099-1112. doi:[10.14358/PERS.72.12.1339](https://doi.org/10.14358/PERS.72.12.1339).
- Yu, X., Hyypää, J., Holopainen, M., and Vastaranta, M. Comparison of area-based and individual tree-based methods for predicting plot-level forest attributes. *Remote Sensing*, 2(6):1481–1495, 2010. doi:[10.3390/rs2061481](https://doi.org/10.3390/rs2061481).
- Yu, X., Hyypää, J., Litkey, P., Kaartinen, H., Vastaranta, M., and Holopainen, M. Single-sensor solution to tree species classification using multispectral airborne laser scanning. *Remote Sensing*, 9(2), 2017. doi:[10.3390/rs9020108](https://doi.org/10.3390/rs9020108).
- Zhang, W., Qi, J., Wan, P., Wang, H., Xie, D., Wang, X., and Yan, G. An easy-to-use airborne lidar data filtering method based on cloth simulation. *Remote Sensing*, 8(6), 2016. doi:[10.3390/rs8060501](https://doi.org/10.3390/rs8060501).
- Zhao, H., Jiang, L., Jia, J., Torr, P., and Koltun, V. Point transformer. In *Proceedings - 2021 IEEE/CVF International Conference on Computer Vision, ICCV 2021*, Proceedings of the IEEE International Conference on Computer Vision, pages 16239–16248. Institute of Electrical and Electronics Engineers Inc., 2021. doi:[10.1109/ICCV48922.2021.01595](https://doi.org/10.1109/ICCV48922.2021.01595).
- Ørka, H. O., Gobakken, T., Næsset, E., Ene, L., and Lien, V. Simultaneously acquired airborne laser scanning and multispectral imagery for individual tree species identification. *Canadian Journal of Remote Sensing*, 38(2):125–138, 2012. doi:[10.5589/m12-021](https://doi.org/10.5589/m12-021).

A Confusion matrices

Figures A.1 to A.3 present the normalised confusion matrices for the trained models.

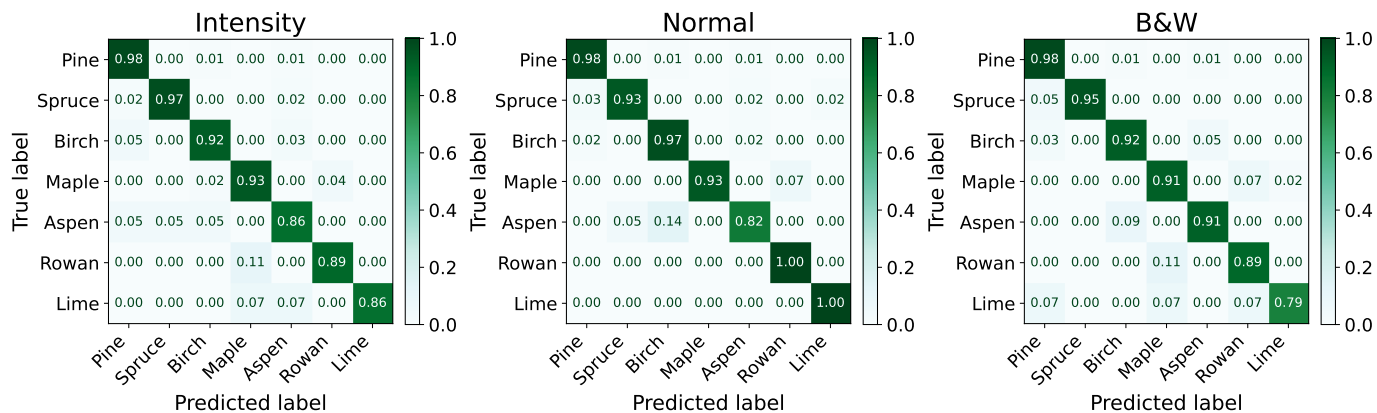
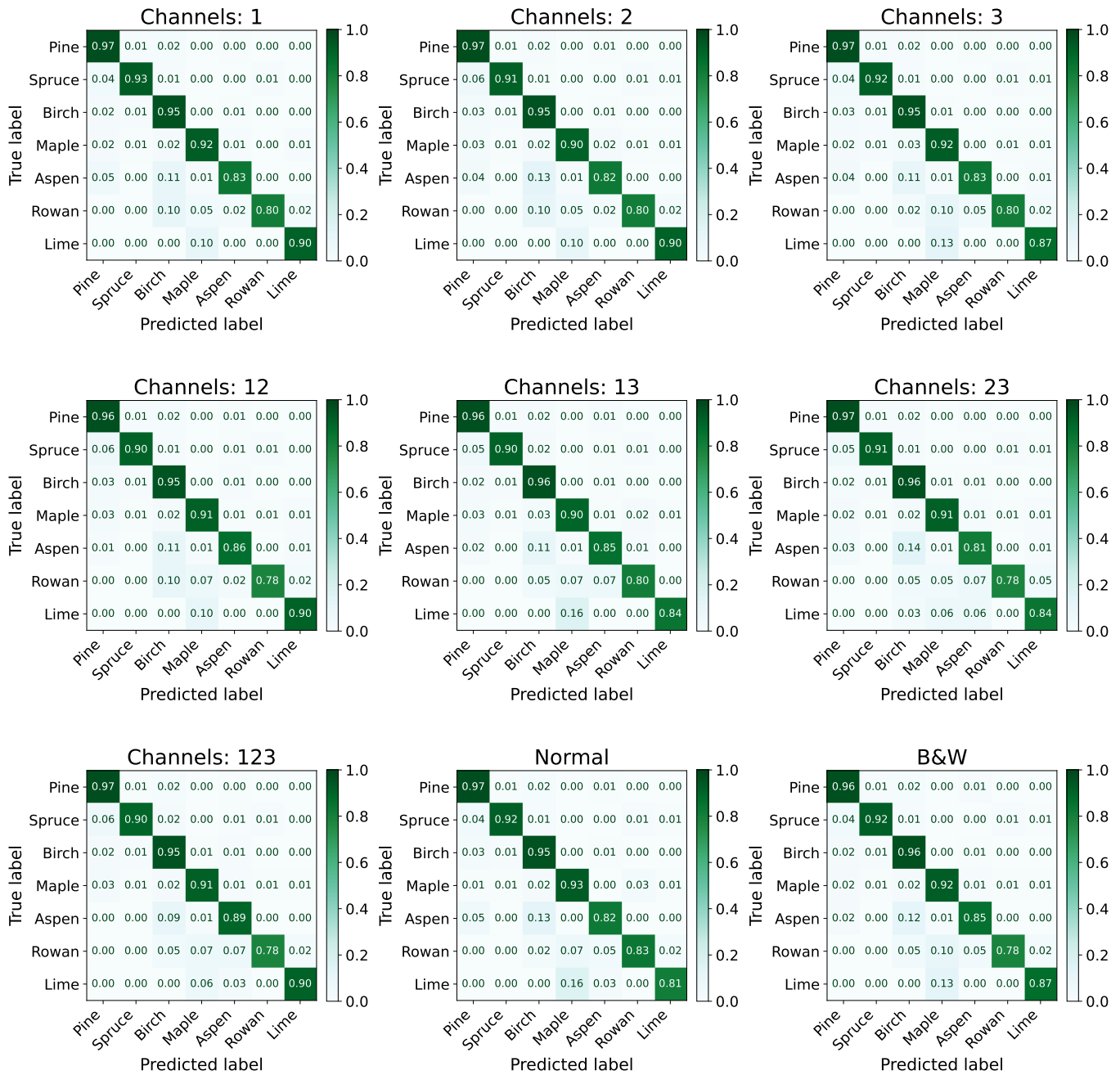


Figure A.1: Normalised MLS confusion matrices



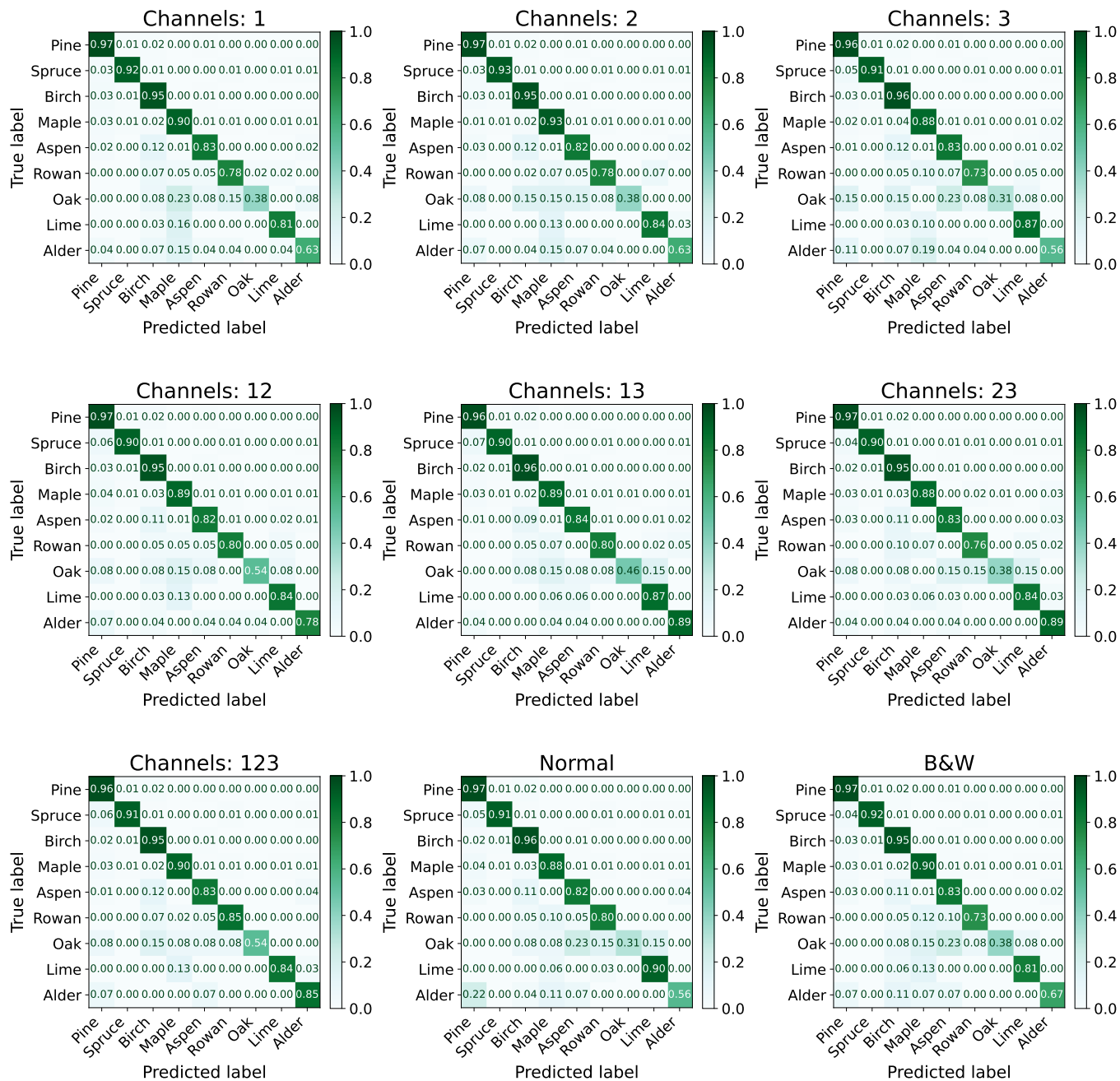


Figure A.3: Normalised confusion matrices (ALS, 9 species)